

OPEN ACCESS

EDITED BY Larry Lyons, University of California, Los Angeles, **United States**

REVIEWED BY Lei Dai, Chinese Academy of Sciences (CAS), China Dae-Young Lee. Chungbuk National University. Republic of Korea

*CORRESPONDENCE Harriet George.

RECEIVED 28 August 2025 REVISED 11 October 2025 ACCEPTED 16 October 2025 PUBLISHED 10 November 2025

CITATION

Hensley AN, George H, Kalliokoski M and Olifer L (2025) Extremely rapid radiation belt electron losses across the magnetopause. Front, Astron. Space Sci. 12:1694836. doi: 10.3389/fspas.2025.1694836

© 2025 Hensley, George, Kalliokoski and Olifer. This is an open-access article distributed under the terms of the Creative Commons Attribution License (CC BY). The use, distribution or reproduction in other forums is permitted, provided the original author(s) and the copyright owner(s) are credited and that the original publication in this journal is cited, in accordance with accepted academic practice. No use distribution or reproduction is permitted which does not comply with these terms.

Extremely rapid radiation belt electron losses across the magnetopause

Alexis N. Hensley¹, Harriet George²*, Milla Kalliokoski³ and Leonid Olifer⁴

¹Physics Department, Berea College, Berea, KY, United States, ²Laboratory for Atmospheric and Space Physics, University of Colorado Boulder, Boulder, CO, United States, ³Department of Physics, University of Helsinki, Helsinki, Finland, ⁴Department of Physics, University of Alberta, Edmonton, AB,

Introduction: The Earth's radiation belt environment is highly dynamic, with different processes acting on various particle populations over a range of timescales. Constraining the timescales over which these processes act is essential to both our physical understanding of the radiation belt environment and our ability to predict and mitigate space weather effects.

Methods: In this study, we leverage the GPS constellation to evaluate a radiation belt dropout that occurred on 14 May 2019, combining observations from 18 GPS satellites during this event to evaluate the dominant loss mechanism of the dropout and to constrain the timescale of this loss. This dropout affected the entire relativistic electron population, abruptly depleting the 4 MeV population by an order of magnitude following a strong magnetopause compression.

Results: We identify magnetopause shadowing as the dominant loss mechanism during this dropout through analysis of the electron flux data and the temporal evolution of the electron phase space density with respect to the last closed drift shell. The $K = 0.14R_FG^{1/2}$, $\mu = 3433MeV/G$ electron population was eliminated within 30 min at $4.8 \le L^* < 4.9$ and eliminated in 126 min at $4.5 \le L^* < 4.6$.

Discussion: Dropout events are typically understood to occur on timescales of several hours to a day and sub-hour dropouts have previously only been reported by a handful of studies, so this is an exceptionally rapid elimination of the relativistic population. Our results therefore reinforce that radiation belt dropouts can occur on sub-hour timescales and highlight the value of the GPS constellation (which now contains 25 satellites distributed across magnetic local time) on studying these rapid, large-scale dynamics in the Earth's radiation belts.

radiation belt, radiation belt dropout, dropout, phase space density, magnetopause

1 Introduction

Earth's outer radiation belt is largely composed of electron populations with energies ranging from 100s keV to multiple MeV, and extends from $\sim 3 < L < \sim 7$ (Turner and Ukhorskiy, 2020). Relativistic (MeV range) outer belt electrons have drift periods on the order of a few minutes. The Earth's outer radiation belt is sensitive to solar wind drivers, such as the impact of coronal mass ejections (CMEs) or high-speed solar wind streams (HSSs), that can cause large, sudden changes to the radiation

belt environment (e.g., Grandin et al., 2019). Thus, the outer radiation belt presents a highly dynamic environment and can undergo system-wide changes in response to solar wind drivers.

The Earth's radiation belts pose a threat to electronics and humans in space, and are therefore a significant space weather hazard (Baker et al., 2017). The outer radiation belt has been highlighted as a particularly severe space weather hazard to spacecraft, including commercial, military and scientific spacecraft (Lanzerotti and Baker, 2017). Satellites that are located on geostationary orbit (equatorial orbits at $\sim 6.6R_F$ geocentric radial distance, where the Earth's radius, R_E , is 6371 km) are nearconstantly exposed to this exceptionally dangerous environment. One particular hazard caused by energetic electrons (≥ 100's of keV) within the outer radiation belt is interior spacecraft charging, where electrons pass through the spacecraft shielding and enter the insulating material within the satellite (Hastings and Garrett, 1996), which can cause an accumulation of charge within the insulating material over time. This accumulated charge induces an electric field and (when this induced field becomes larger than the breakdown strength of the material) a discharge will occur (Hastings and Garrett, 1996). These discharges can be particularly harmful to satellites because they can damage supposedly-shielded materials and sensitive electronics within the spacecraft (Baker et al., 2017). Accurate and timely prediction of the radiation belt environment is critical to mitigating these hazards, as discussed in Horne et al. (2021), but the dynamic environment of the outer radiation belt (particularly in response to extreme driving solar wind conditions) makes this task profoundly difficult. Constraining the timing and driving mechanisms of system-wide radiation belt dynamics is critical for this space weather forecasting that is required to mitigate the hazards presented by the radiation belts.

Radiation belt dropout events are characterized by permanent losses of radiation belt electrons, where the flux of a given population is significantly depleted or even eliminated (e.g., Turner et al., 2012). Precipitation into the atmosphere is a major pathway for the loss of radiation belt electrons. Wave-particle interactions that drive pitch-angle scattering are a major driver of precipitation; plasmaspheric hiss precipitates 10s - 100s keV electrons (Li et al., 2019; Ma et al., 2021) and electromagnetic ion cyclotron (EMIC) waves can drive precipitation of 100s keV to multi-MeV electrons (Usanova et al., 2014; Hendry et al., 2017). Radiation belt losses can also occur when particles cross the magnetopause during their drift orbit and are lost to the solar wind. This can be caused by inward motion of the magnetopause (Cohen et al., 2017; Staples et al., 2022) or outward motion of radiation belt particles (Ozeke et al., 2017; Ozeke et al., 2020; George et al., 2022). The subsolar magnetopause is generally located $11.0R_E$ geocentric distance from Earth (Fairfield, 1971), but can move inward in periods of southward interplanetary magnetic field (IMF) or high dynamic pressure (Shue et al., 1998). The magnetopause can also be strongly compressed when solar wind transients, such as CMEs, impact the Earth's magnetosphere (e.g., Fu et al., 2025), which can directly drive strong losses of radiation belt particles.

Determining the dominant loss mechanism(s) and the timescale of loss during dropout events is critical for understanding these system-wide disruptions to the radiation belt environment. Dropout events may be predominantly caused by precipitation (e.g., Pham et al., 2017), dominated by loss across the magnetopause

(e.g., Olifer et al., 2018), or due to a balance of these two loss pathways (e.g., Xiang et al., 2017). Statistical analysis of 1.1-1.5 MeV radiation belt electron dropouts that were driven by solar wind transients had an average loss time of 6 h (Borovsky and Denton, 2009). A large amount of recent radiation belts research on dropout events (e.g., Turner et al., 2014; Xiang et al., 2018) was performed using the Van Allen Probes (RBSP) constellation, which consisted of a pair of satellites with approximately 8 h orbital periods. RBSP data revealed that radiation belt dropout events generally occur on a timescale of a few hours (Turner and Ukhorskiy, 2020, and references within). For example, one dropout event during the RBSP era caused the relativistic electron population to be lost in <6 hours following the impact of an interplanetary shock, as determined from in-situ RBSP data (Zhang et al., 2016); the dropout timescale for this event was then further refined to ~ 1.5 hours with the use of simulations (Su et al., 2017).

However, a small number of radiation belt dropouts have been identified that occurred significantly faster than this fewhour timescale. Through analyses that combined in-situ data from multiple constellations and/or satellite constellations that dwell within the radiation belts, a few radiation belt dropout events were found to have occurred on sub-hour timescales. As an extreme example, Kurita et al. (2018) reported that an order of magnitude loss of ~2.5 MeV radiation belt electrons due to EMIC-driven precipitation may have occurred in as little as 10 min, comparable to the drift period of MeV electrons in the outer belt. In-situ observations of radiation belt dynamics on this timescale are highly challenging; Kurita et al. (2018) leveraged data from the two RBSP satellites and Arase satellite, which observed an order of magnitude flux decrease of the ~ 2.5 MeV electron population within ~ 1.5 hours during a period of enhanced EMIC activity. Combining these in-situ observations with the onset time of ground-based observations of detached proton aurora (a proxy for the start time of EMIC-driven precipitation) provided a ~ 10 minute timescale of the radiation belt dropout (Kurita et al., 2018). The Global Positioning System (GPS) constellation has also been used to evaluate systemwide radiation belt dynamics that occur on timescales shorter than the RBSP orbital period, as the multiple satellites within this constellation are distributed across magnetic local time (MLT) and therefore provide global observations of the radiation belt environment. Olifer et al. (2018) used GPS observations to evaluate several radiation belt dropouts and determined that these events had $a \le 0.5 - 2$ hour loss timescale, and that these rapid radiation belt dropouts were driven by sharp compression of the magnetopause. Morley et al. (2010) also examined a rapid radiation belt dropout using GPS data, and determined that the loss timescale was ~2 hours. Strong outward radial diffusion can continually transport radiation belt electrons beyond the magnetopause in the aftermath of the initial depletion (Loto'aniu et al., 2010), which can cause the dropouts to persist for long timescales following a rapid loss, such as a ≥ 10 days extinction of the multi-MeV electron populations following a loss event that depleted the outer belt in approximately an hour (Ozeke et al., 2017).

In this study, we evaluate a rapid radiation belt dropout that occurred on 14 May 2019, using observations of outer radiation belt electrons from the GPS constellation. We find that the 4 MeV electron population was totally eliminated in 30 min at $4.8 \le L^* < 4.9$, which is an intense and extremely rapid dropout, and determine

that this dropout was driven by losses across the magnetopause. Section 2 describes the data used in this study, Section 3 provides an overview of the dropout event, and Section 4 details our analysis of the radiation belt fluxes and phase space density (PSD). The conclusions of this study are in Section 5.

2 Data and methods

2.1 GPS electron flux data

We use electron flux data (j) provided by the GPS constellation, which consisted of 21 satellites in 2019. These satellites are distributed across six orbital planes with near-circular orbits of a constant geocentric average distance of $4.17R_E$ (Morley et al., 2010). The six orbital planes have a nominal inclination of 55° and are distributed across magnetic local time (MLT) with a 12-h orbital period (Morley et al., 2016). The highly tilted orbits of the GPS satellites mean that they cross magnetic field lines corresponding to a wide range of L-shell (L). At the equator, the GPS sample particles near L \sim 4 and at greater latitudes, measure particles bouncing along the magnetic field lines corresponding to higher L-shells. Therefore, the GPS constellation provides observations at L-shells through the mid-outer portions of the outer radiation belt.

We utilize data from all active satellites that carry a Combined X-ray Dosimeter (CXD) instrument during the 14 May 2019 event, except ns60, ns69, and ns74 for a total of 18 satellites. The CXD instrument provides omnidirectional electron counts with a 4min time resolution. The electron count data from GPS satellites were calibrated against Van Allen Probe (RBSP) data during satellite conjunctions to derive a flux data product; a summary of the calculation of electron fluxes from GPS observations is provided in Morley et al. (2016). Satellite ns60 had intermittent noise during this event that resulted in unreliable flux fit modeling so was removed from the analysis; Smirnov et al. (2020) and Kalliokoski et al. (2023) also removed satellite ns60 from their analysis of 17 years due to long-term intermittent noise. Satellite ns69 was removed due to lowquality fits. Satellite ns74 was removed from the analysis because the dropped_data quality flag indicates that this satellite had poorquality data from midnight until 11:00 UTC. As a result, ns74 did not provide observations within the radiation belts before the dropout or during the initial stages of the dropout itself, making it unsuitable for our analysis.

We use version v1.10 of the GPS data. We use the 4.0 MeV electron fluxes included in the GPS data product for this study and L-shell calculated with the (Tsyganenko, 1989, T89) magnetic field model combined with the International Geomagnetic Reference Field (IGRF, Alken et al., 2021) internal field.

We use the fit quality flag (F, Equation 1) defined in Smirnov et al. (2020), where the predicted and observed:.

$$F = \max\left(\left|\log_{10} \frac{\text{predicted counts}}{\text{observed counts}}\right|\right),\tag{1}$$

where the predicted and observed counts are provided by the variables "model_counts_electron_fit" and "rate_electron_ measured" respectively in the GPS datafiles. We remove any flux datapoints where F > 0.11 to remove low quality fits, as was also used by Smirnov et al. (2020), Kalliokoski et al. (2023), Olifer et al.

(2024). The ns69 satellite had F > 0.11 throughout the dropout event so was removed from our analysis.

2.2 Phase space density calculation

Evaluation of flux data to determine the mechanism(s) driving radiation belt dynamics can sometimes be misleading, as adiabatic changes (such as the Dst effect, Kim and Chan, 1997) can drive large variations in the flux data without fundamentally changing the population. To overcome this limitation, many radiation belt studies (e.g., Reeves et al., 2013; Turner et al., 2014; Dai et al., 2015; Zou et al., 2020; Drozdov et al., 2022) evaluate the phase space density (PSD, f) of a population. The PSD of a population [when expressed in terms of adiabatic coordinates, μ , K and L^* , detailed in Koskinen and Kilpua (2022)] does not temporally vary as the population undergoes adiabatic processes, so analysis of PSD data can isolate the non-adiabatic processes acting on a given radiation belt population. Evaluation of the PSD of a radiation belt population therefore enables determination of the dominant process (es) that drive permanent changes to that population.

The electron phase space density can be calculated from the electron flux. Electron flux data are generally provided as a function of energy (E), pitch angle (α) and L-shell (L). Liouville's theorem states that f can be calculated in terms of E and α by dividing $j(E,\alpha)$ by the relativistic momentum squared of the population. Coordinate changes are then used to transform the E0 of the flux observation into the corresponding E1, and then E1, E2 of the population into the E3. Further detail on these coordinate transforms are provided in Section 2.1 of Olifer et al. (2024). The calculation of E3 and E4 from E1, E3 and E4 requires the use of a global geomagnetic field model; we use the Tsyganenko and Sitnov (2005) (TS04) model for these calculations.

We calculate the electron phase space density from the GPS data following the approach of Hartley and Denton (2014), which has previously been applied to the GPS data in Kalliokoski et al. (2023), Olifer et al. (2024). In order to calculate the electron PSD from the GPS flux data, we first select the μ and K values for the population of interest; we select $K = 0.1R_EG^{1/2}$, $\mu = 3433$ MeV/G population for analysis in this study. We then use the LANLGeoMag library (Henderson et al., 2018) and TS04 geomagnetic field model to calculate the equatorial pitch angle corresponding to the selected K at the satellites' locations, and the L^* corresponding to these locations. Next, we calculate the energy of the population corresponding to this equatorial pitch angle and L^* . The selected μ , Kvalues correspond to an electron population with energy of ~ 3.5 MeV and equatorial pitch angle of $\sim 50^{\circ}$ at $L^* \sim 4.2$. We then use the flux-forward model (Henderson et al., 2018) to calculate the omnidirectional electron flux at this energy from the GPS count data. This flux-forward model is a fit to a combination of relativistic Maxwellian and Gaussian functions, and the fit parameters are provided in the GPS data product; further details on this model are provided in the appendix of Morley et al. (2010).

The next step of the PSD calculation combines the omnidirectional electron flux data corresponding to the selected μ , K with a pitch angle distribution model in order to acquire the directional flux. We use the relativistic electron pitch angle

distribution (REPAD, Chen et al., 2014) model for this calculation. This is an empirical model that was developed from statistical analysis of pitch angle distributions of relativistic electrons in the outer radiation belt, using data from CRRES, Polar and LANL-97A, and was constructed by fitting Legendere polynomials to the observed pitch angle distributions. The REPAD requires parameters from the magnetic field model and AE index as input; the AE data were accessed from OMNIWeb (https://omniweb.gsfc.nasa.gov/, last access: 2 Feb 2024) and we again use the TS04 model for the inputs to REPAD. The equatorial pitch angle distribution obtained from REPAD were then normalised by the omnidirectional flux data from GPS, providing the directional fluxes for the equatorial pitch angles and energies corresponding to the selected μ and K values. This provides the $j(E, \alpha)$ for the electron population with the selected μ , K at each L where electron counts are observed by a given GPS satellite. This $j(E,\alpha)$ can then be converted to $f(E,\alpha)$ by dividing by relativistic momentum squared to obtain the PSD at each L and time. Coordinate transforms then express these data in adiabatic coordinates to obtain $f(\mu, K, L^*)$.

The use of a pitch angle model to calculate the directional fluxes from the omnidirectional flux data introduces some uncertainty. When a GPS satellite is near the magnetic equator, the counts measured by the CXD instrument will encompass a large majority of the electron population, including the particles with very large equatorial pitch angles that mirror near the equator. However, as the satellite moves away from the equator, the GPS count data will represent a smaller and smaller portion of the total population, as the CXD will only be able to detect electrons that have a magnetic mirror point that is located at a magnetic latitude that is greater than the latitude of the satellite. As a consequence, the GPS count data at large L does not include the full particle distribution but only includes particles with sufficiently small equatorial pitch angles to mirror beyond the satellites' location. The uncertainty of the directional flux data that corresponds to near-equatorially mirroring particles is therefore larger when the satellite is located at high L. In order to combat this uncertainty, we calculate the ratio between the portion of the pitch angle distribution that is observed by the GPS satellite and the full pitch angle distribution, and discard PSD data where this ratio is less than 10%. This is the same uncertainty evaluation that was used in Kalliokoski et al. (2023).

2.3 Solar wind and geomagnetic conditions

We use solar wind and interplanetary magnetic field (IMF) data accessed from the OMNI database (Papitashvili and King, 2020) to contextualize the radiation belt dropout event. We use the 1-min time resolution data from the WIND spacecraft that was timeshifted from the L1 point to the subsolar bowshock nose. We also use planetary K-index (K_p) and Disturbance Storm Time (Dst) indices from ground-based observations accessed via WDC Kyoto. Finally, we calculate the Last Closed Drift Shell (LCDS) from the LANLGeoMag model (Henderson et al., 2018). The LCDS is the maximum defined L^* of a population with given a K value, and therefore represents the outer boundary of stable trapping in the Earth's radiation belts (Albert et al., 2018). We compute the LCDS for the $K=0.14R_EG^{1/2}$ population using the TS04 geomagnetic field model.

3 Event overview

Solar wind/IMF conditions and geomagnetic indices are shown in Figure 1 to contextualize the radiation belt dropout that occurred on 14 May 2019. Figure 1a shows the IMF components and magnitude, subplot 1b depicts the solar wind dynamic pressure, and subplot1c provides the solar wind velocity. Subplot 1d shows the K_p and Dst geomagnetic indices. Subplot 1e shows the magnetopause location calculated from the Shue et al. (1998) magnetopause model (R_E), and subplot 1f shows the LANLGeoMag LCDS calculated with $K=0.14R_EG^{1/2}$ and the TS04 geomagnetic field.

The solar wind velocity steadily increases from ~400 km/s at midnight until ~5:00 UTC (all times are in UTC and 24-h time for the remainder of the manuscript), at which point it plateaued at a value of 550 km/s for the remainder of the 14 May 2019. The continuous 550 km/s solar wind velocity classifies this event as a HSS (Grandin et al., 2019). In addition to the high solar wind velocity, there is also a strong southward IMF on the morning of 14 May 2019. Figure 1a shows that the IMF magnitude (blue) was elevated and that the southward $(B_z, \text{ red})$ component dominated. From approximately 4:00-7:00, the B_z component plateaued at ~ -10 nT while the total IMF magnitude was ~ 12 nT. The magnetic field would then be further amplified following transmission across the bowshock before impinging on the Earth's magnetopause (Dai et al., 2023; Madanian et al., 2024) A large dynamic pressure pulse (magnitude ~ 8 nPa) then occurred as the IMF rotated northward from ~7:00-8:00, following which the IMF magnitude decreased and the B_z component remained near 0 nT. Moreover, the DST reaches a minimum value of -65 nT and K_p reaches a maximum of 6.3, corresponding to a moderate geomagnetic storm, with the strongest geomagnetic activity occurring from 6:00-9:00.

Negative IMF B_z and high solar wind dynamic pressure result in effective dayside magnetopause reconnection (Milan et al., 2006). Enhanced dayside reconnection can directly result in enhanced magnetospheric convection (Dai et al., 2024) and erosion of the subsolar magnetopause (Cowley and Lockwood, 1992). The subsolar magnetopause location (R_{mp}) calculated from the Shue et al. (1998) model is shown in Figure 1e; this is strongly compressed from 4:00-8:00. The magnetopause is initially located at ~ $10R_E$ at the beginning of the day, but rapidly undergoes a strong compression to \sim 7–8 R_E beginning at approximately 4:00 when the IMF rotates southward. The magnetopause remains continuously compressed until ~8:00, when the magnetopause quickly returns to its pre-compression location of ~10 R_E . The compression of the magnetopause closely aligns with the time period where the IMF was predominantly southward with comparatively minor B_x and B_{ν} components; the dynamic pressure pulse at ~7:00 had a comparatively minor effect on the magnetopause location.

The LCDS, which represents the outer boundary of trapped outer radiation belt particles in adiabatic space (Albert et al., 2018), also demonstrates a strong compression from $L^* \sim 8$ at 4:00 to $L^* \sim 5.5$ at 7:00. The LCDS then begins to move to higher L^* at approximately 8:00 and returns to its nominal location by 12:00. The LCDS compression was more gradual than the inward motion of the magnetopause determined from the Shue et al. (1998) model, but the timing of the LCDS compression onset closely aligns with the magnetopause compression. Therefore, the outer boundary of the outer radiation belt, demonstrated by both the magnetopause model

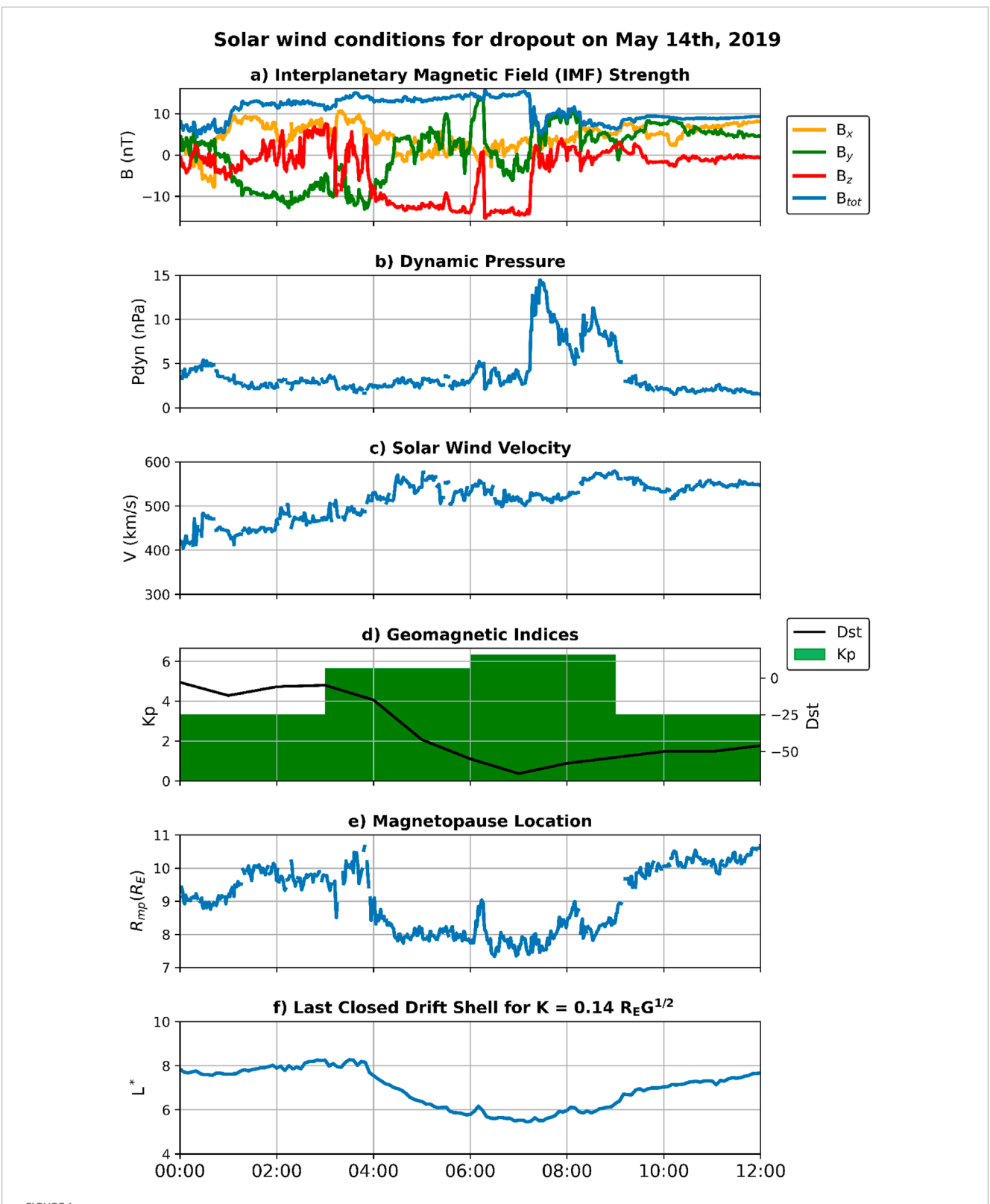


FIGURE 1 Solar wind driving conditions during the radiation belt dropout event. (a) Interplanetary Magnetic Field (IMF) strength and components. (b) Solar wind dynamic pressure. (c) Solar wind velocity. (d) K_p and DST indices. (e) Subsolar magnetopause location. (f) LCDS calculated with $K = 0.14R_EG^{1/2}$ and the TS04 geomagnetic field. The x-axis displays the time in UTC.

and the LCDS, moved significantly inward at approximately 4:00 and remained compressed for several hours before beginning to recover.

4 Results

4.1 Radiation belt fluxes

Figure 2 shows the combined flux data from all 18 GPS satellites on 14 May 2019 for relativistic electron populations at energies ranging from 0.8–4 MeV. These data are binned over 30 min and 0.2 L, with the mean value taken when multiple data points fall within a given time and L-shell bins, with different subplots corresponding to different energies in the relativistic range. White bins indicate time/L-shell bins that did not contain any data. The Shue et al. (1998) magnetopause model is overlaid in black (unit R_E) on each subplot and corresponds to the right y-axis. We observe that the dropout event affected a broad range of relativistic electron populations and hereon focus our analysis on the 4 MeV electron population.

Figure 2 spans the time period from noon May 13 until the end of 15 May 2019 to contextualise the dropout event with respect to the pre-dropout conditions and recovery phase. There are steady fluxes for the afternoon of May 13 and early morning of May 14, with comparatively minor temporal variations in the 4 MeV electron population. These fluxes are greatest between \sim 4.5–6 L-shell and peak at $L \sim$ 5. An abrupt dropout then occurs at approximately 4:00, corresponding to the time of strong inward compression of the magnetopause and beginning of the inward motion of the LCDS. The electron fluxes at L-shell >6 are strongly depleted at this time, with either extremely low (< ~ 10⁰ cm⁻²sec⁻¹sr⁻¹MeV⁻¹) fluxes or the absence of electron flux observations (demonstrated by the white boxes). The electron fluxes at $4 \le L \le 6$ decrease by approximately two orders of magnitude after 4:00, from approximately 10² cm⁻²sec⁻¹sr⁻¹MeV⁻¹ to 10⁰ cm⁻²sec⁻¹sr⁻¹MeV⁻¹. The dropout persists for several hours and then begins to recover at L-shell ≤ 6 at approximately 8:00. The magnitude of the electron fluxes returns approximately to the predropout value, but with the strongest fluxes now located at L-shell < 5. The electron fluxes at L-shell > 6 remain strongly depleted for the remainder of the day. The different phases of the dropout event are illustrated by the colored bars at the top of each subplot with 1h precision: blue corresponds to the pre-dropout conditions, orange highlights when the dropout itself occurred, and green corresponds to the recovery period.

To more thoroughly evaluate the spatial and temporal evolution of the radiation belt dynamics during the dropout itself, we examine the observations of single GPS satellites during the dropout. Figure 3 shows the 4 MeV flux data as a function of time and L-shell from selected satellites (ns67, ns72, ns65, and ns64 respectively) during this event. The color scale shows the magnitude of the electron flux, and each subplot uses the same color bars to enable direct comparison of the electron fluxes observed by each satellite. GPS satellites are distributed along four orbital planes, and therefore sample different L-shell at different times; we selected representative examples of satellites on different orbital planes to show in Figure 3. While instrumentation limitations of the GPS satellites means that a quantitative comparison of the flux data

from different satellites is not always meaningful, the different orbital trajectories of these satellites allows us to qualitatively evaluate the outer radiation belt fluxes at different phases of the dropout event and the timing of the dynamics with respect to the magnetopause location. Please note that Figure 3 shows the flux observations by individual satellites over a shorter, 12 h time frame than Figure 2.

The pre-dropout fluxes are shown by complete passes of ns67 (subplot a) and ns64 (subplot d), and partial passes of ns72 (subplot b) and ns65 (subplot c) prior to 4:00. The fluxes observed by each satellite are approximately temporally constant at a given L-shell until ~4:00, at which point the strong magnetopause compression occurs. The outer radiation belt fluxes at the time of the magnetopause compression are most clearly shown by ns65, as its orbital trajectory means that this satellite is located at $L \sim$ 4.8 for almost an hour around the time of the magnetopause compression. There is a steady flux decrease at $L \sim 4.8$ over this time period, and, as ns65 moves to higher L-shell from 5:00-6:00, the fluxes observed at a given L are lower than the fluxes at the same L prior to the magnetopause compression by nearly an order of magnitude. Satellite ns64 then provides observations of the outer radiation belt fluxes during the second half of the magnetopause compression: the fluxes observed by ns64 during this period are one to two orders of magnitude lower than the ns64 flux observations at a given L prior to the magnetopause compression. The radiation belt fluxes quickly recover following the expansion of the magnetopause back to its original position; ns67 shows comparable fluxes at $L \sim 4.5$ at 2:30 and 8:00, which is soon before the abrupt magnetopause compression and after the magnetopause relaxation.

These GPS flux data demonstrate that the 4 MeV electron population experienced a strong dropout that began at approximately 4:00 on 14 May 2019 and lasted for approximately 4 hours before beginning to recover around 8:00. Analysis of the radiation belt fluxes observed by individual GPS satellites distributed along different orbital planes demonstrates that the dropout onset closely corresponds to the beginning of the strong compression of the magnetopause, with the recovery of the radiation belt fluxes also corresponding to the relaxation of the magnetopause to its nominal location. This close timing correlation between the radiation belt flux dropout/recovery and the magnetopause compression/relaxation is a strong indicator that significant loss across the magnetopause occurred during this event.

Relativistic radiation belt electrons can also be lost via precipitation to the atmosphere by pitch-angle scattering driven by electromagnetic ion cyclotron (EMIC) waves (Usanova et al., 2014). EMIC-driven losses are characterised by the near-simultaneous precipitation of high energy electrons and low energy protons (Carson et al., 2013). Algorithms to detect relativistic electron precipitation (REP) signatures have been developed for the Polar Orbiting Environmental Satellites (POES) satellites (Hendry et al., 2016) and CALET instrument onboard the International Space Station (ISS) (Vidal-Luengo et al., 2024). Neither algorithm detected REP signatures during the dropout event on 14 May 2019, although we note that the CALet algorithm detected 5 REP events between 7:20 and 8:56 on this date. These precipitation signatures did not occur during the dropout itself but rather began during the recovery phase when there were more relativistic radiation belt electrons

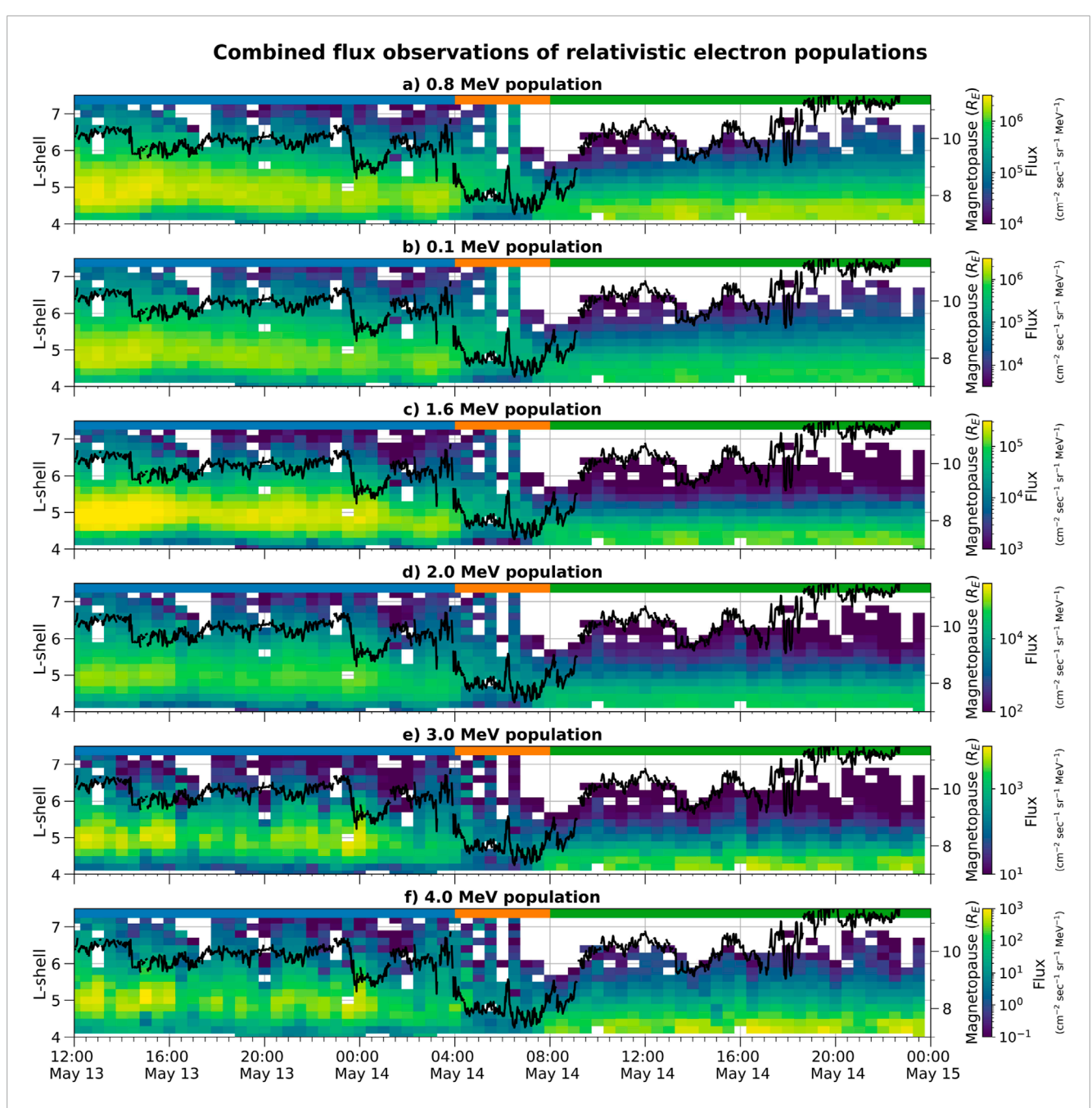
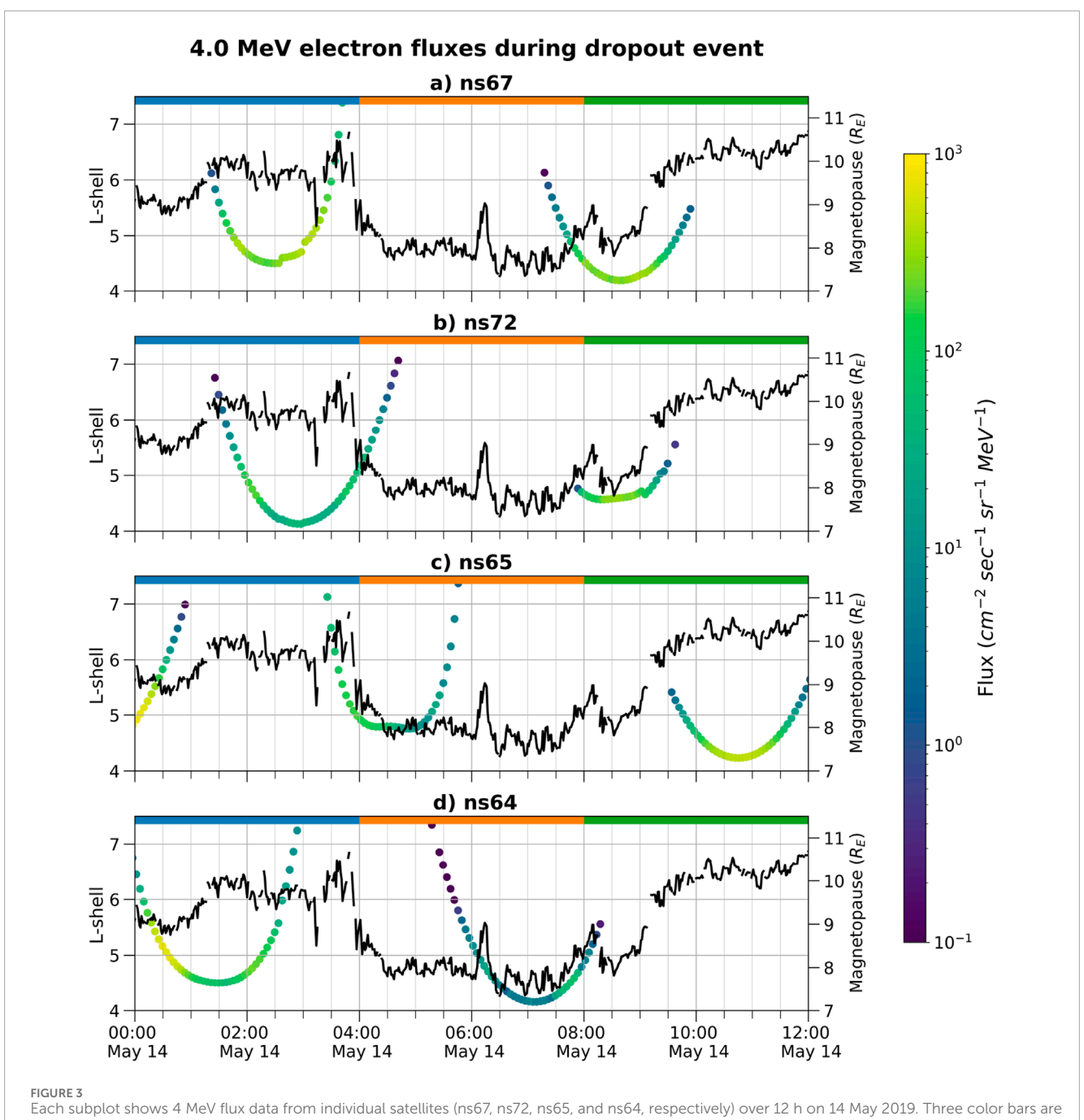


FIGURE 2
Combined GPS satellite observations of the 0.8, 1.0, 1.6, 2.0, 3.0, and 4.0 MeV electron fluxes, compiled from 18 satellites, spanning from noon on May 13 to the end of 14 May 2019, with the Shue et al. (1998) magnetopause model overlaid in black. The magnetopause model corresponds to the righ y-axis. On each subplot, there are three color bars illustrating the different stages of the event, with the start and end times of the event stages estimated to 1-h precision. Blue represents the pre-dropout stage, the orange color bar represents the dropout itself, and the green color bar represents the post-dropout (recovery) period. Note that the colour scale varies between subplots. (a) 0.8 MeV population, (b) 0.1 MeV population, (c) 1.6 MeV population, (d) 2.0 MeV population, (e) 3.0 MeV population, (f) 4.0 MeV population.

available to be precipitated at low L-shell. Visual inspection of the POES data indicated that multiple REP events may have occurred between midnight and 8:00 on May 14, which encompasses both the dropout event and a 4-h period prior to the dropout onset, although a high level of background proton precipitation resulted in non-detection of REP events by the algorithm. It is therefore possible that a combination of EMIC-driven precipitation and losses across the magnetopause occurred on 14 May 2019, despite the lack of

unambiguous REP detections from either CALET or POES during the dropout event. However, the presence of possible REP events for 4 hours prior to the dropout in combination with the sudden dropout onset means that it is unlikely that precipitation was the driving loss mechanism of this dropout, while losses across the magnetopause are significantly more likely due to the close timing correlation between the magnetopause compression and the onset of the dropout.

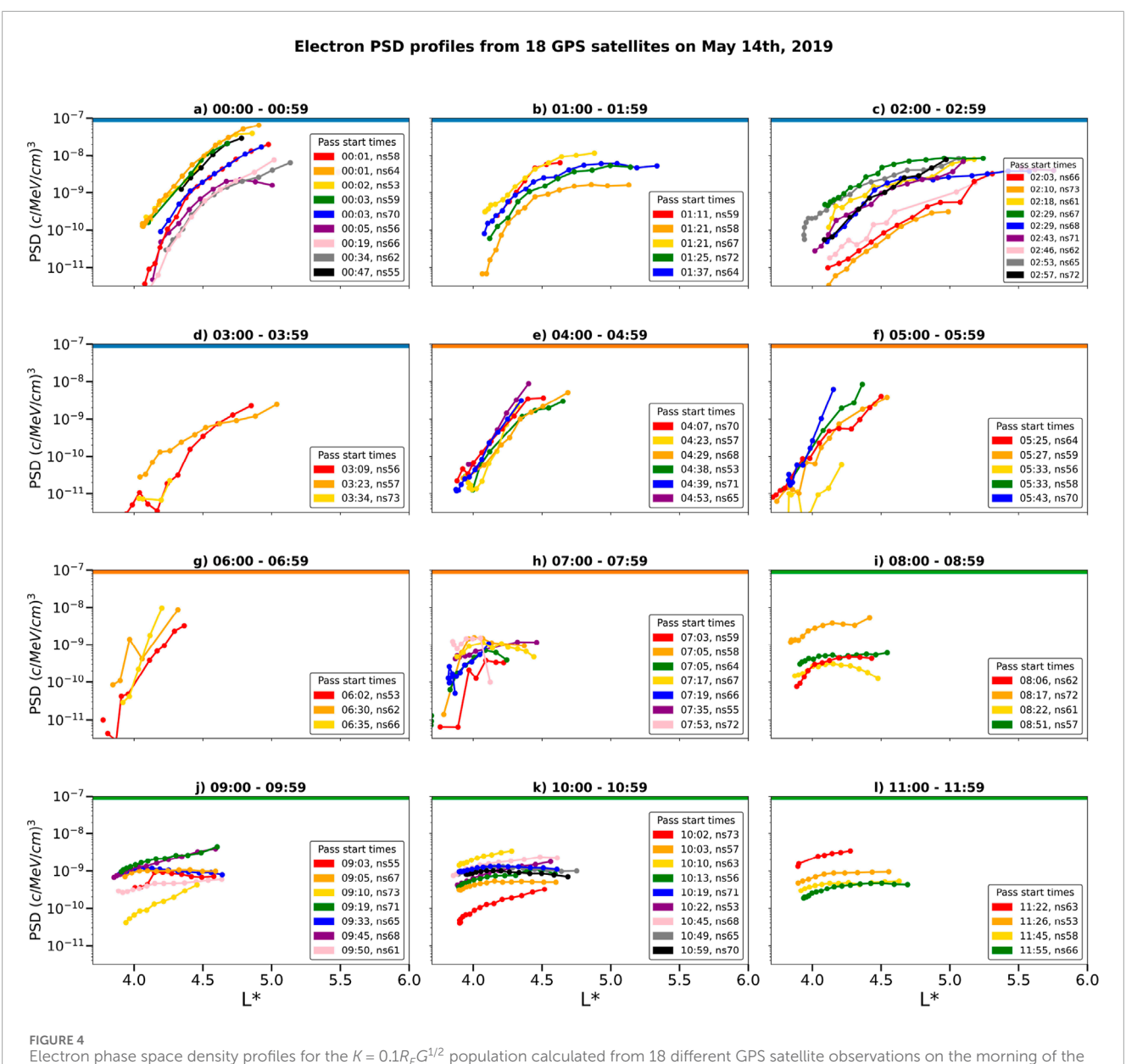


Each subplot shows 4 MeV flux data from individual satellites (ns67, ns72, ns65, and ns64, respectively) over 12 h on 14 May 2019. Three color bars are shown at the top of each subplot to represent the three main phases of the dropout event, in the same way as Figure 2. (a) ns67, (b) ns72, (c) ns65, (d) ns64.

4.2 Phase space density results

To constrain the timing of the dropout event and further evaluate the driving mechanism by which the radiation belt electrons were lost, we investigate the temporal evolution of the electron PSD. Figure 4 shows the electron PSD profiles for 18 satellites organized by their pass start times. The PSD is calculated from the GPS electron flux data combined with the TS04 geomagnetic field model and the REPAD model for the population with $K = 0.1R_E G^{1/2}$, $\mu = 3433 MeV/G$. Each subplot shows the PSD

profiles for a single hour on 14 May 2019, and the red profile in each subplot shows the PSD profile with the earliest start time within that hour, moving to blue or purple for later observations. Each PSD profile corresponds to the observations from a single satellite, and each dot indicates a single data point (which has time uncertainty of \pm 2 min). The satellite vehicle number and start time of a given PSD profile is provided in the legend of each subplot. The horizontal bar at the top of each subplot shows the stage of the event as identified from the flux data, with blue, orange and green corresponding to the pre-dropout, dropout and recovery phases respectively.



Electron phase space density profiles for the $K = 0.1R_EG^{1/2}$ population calculated from 18 different GPS satellite observations on the morning of the dropout event. Each subplot shows a different hour and the color of each profile corresponds to the timing of the pass, with red PSD profile corresponding to the first profile within a given hour. All times are in UTC. (a) 00:00-00:59, (b) 01:00-01:59, (c) 02:00-02:59 (d) 03:00-03:59, (e) 04:00-04:59, (f) 05:00-05:59 (g) 06:00-06:59, (h) 07:00-07:59, (i) 08:00-08:59, (j) 09:00-09:59, (k) 10:00-10:59, (l) 11:00-11:59.

Prior to the magnetopause compression and the radiation belt dropout at $\sim 4:00$, the electron PSD profiles extend to $L^* \sim 5.2-5.5$ (subplots 4 a-c). The shape and spatial extent of the PSD profiles calculated from flux data obtained from different satellites are similar at a given time over this period; variation in the magnitude of the PSD between different satellites can clearly be seen but is likely due to instrumentation variations and not system-wide changes in the radiation belt environment, as Figure 2 showed a relatively constant radiation belt environment at this time. These PSD profiles peak at $L^* \sim 4.5-5.0$ and have the lowest value at $L^* \sim 4$. There is a slight flattening of the PSD profile between midnight and $\sim 3:30$ (compare the red profile, ns58, in Figure 4a to the orange profile, ns57, in Figure 4d), indicating that radial

diffusion may be acting on the population. However, both the PSD and the electron fluxes (Figure 2) show relatively little temporal variation over this time period, demonstrating that the radiation belt environment was in a relatively stable state until 4:00, which is consistent with the flux observations.

In subplot 4e, which shows the observations from 4:00–4:59, the PSD profiles exhibit a distinct change from the earlier profiles. The PSD profiles in Figure 4e show a significantly steeper gradient than those from earlier in the day, and also span a shorter L^* range; the most distant data points between 4:00–4:59 are located at $L^* \sim 4.7$, which is significantly further Earthward than the earlier profiles that generally extended to $L^* \sim 5.5$. This demonstrates that the radiation belts have undergone a large, non-adiabatic

change around 4:00 that caused by an abrupt, irreversible loss at $L^* \ge 4.7$.

The steep PSD gradient persists until the pass that begins at 6:30 (orange profile, ns62, subplot 4g). These PSD profiles are characteristic of loss at the outer boundary (i.e., across the magnetopause) that suddenly and permanently removed the particles at high L^* . Strong gradients in PSD profiles then enable highly effective radial diffusion (Bentley et al., 2024), which would act to rearrange the radial distribution of the PSD. The persistence of these steep profiles for several hours indicates that the loss across the magnetopause continues throughout this time period and that this loss dominates over radial diffusion to control the overall radiation belt dynamics.

The PSD profile begins to flatten after 7:00, as observed by ns59 and shown in red in subplot 4 h. The innermost four data points, observed at 7:03-7:31 show a steep gradient, consistent with the earlier PSD profiles. The outermost three data points observed by ns59 in this pass, observed at 7:35, 7:39 and 7:43, form a distinctly flatter profile, indicating that the loss across the magnetopause is no longer dominating the system and the radial diffusion has begun to flatten the PSD profile. The other passes that began between 7:00-7:59 show the same flattening of the PSD profile; the ns55 pass, for example, that is shown in purple in subplot 4 h has an extremely shallow gradient. This PSD evolution from a steep gradient to a near-flat profile is characteristic of strong radial diffusion that acts relatively quickly to completely rearrange the outer radiation belt electrons. The flat PSD profiles then persisted for several hours; Figure 4 shows these profiles until noon and Supplementary Figure S1 in the Supplementary Material shows the PSD profiles in the same format from noon until midnight on May 14th. This evolution of the PSD profiles and the near-flat PSD profiles (see Figure 4l in particular) demonstrate that radial diffusion dominated the radiation belt dynamics from ~ 7:00 onward.

The dynamics of the PSD profiles are tightly correlated with the timing of the magnetopause and LCDS compression and relaxation, shown in Figure 1e. The PSD extends over a broad L^* range with a stable configuration until approximately 4:00. The time of the change in the PSD profiles (from peaking at mid- L^* and extending to high L^* , to a sharp gradient that is truncated in L^*) corresponds to the time of the magnetopause compression and onset of the flux losses (Figure 2). As discussed earlier, we can not eliminate EMIC driven precipitation as a loss mechanism during this event, but the PSD profiles do not indicate that precipitation was a significant loss mechanism during this dropout event. Therefore, based on the temporal evolution of the PSD profiles combined with the close timing correlation to the magnetopause and LCDS location, we identify magnetopause shadowing as the dominant loss mechanism during this event.

Figure 5 shows the PSD data in selected L^* ranges over the 12 h period during which the dropout occurred in comparison to the LCDS computed with $K = 0.14R_EG^{1/2}$. We evaluate the temporal evolution of the PSD in specific L^* ranges with respect to the LCDS, which is calculated in adiabatic space (as a function of L^*), and calculate how long it takes for the population to be eliminated following the LCDS compression at a given L^* , which we define as the dropout timescale. This enables a more direct comparison between the temporal evolution of the PSD and the radiation belt outer boundary than with a magnetopause model, which is in units

of physical distance and not adiabatic space. Each subplot shows the PSD in a different L^* range; subplot 5a) shows the PSD at L^* between the ranges of 4.8–4.9, subplot 5b shows PSD at L^* from 4.5 to 4.6, and in subplot 5c corresponds to PSD at L^* between 4.2–4.3.

Figure 5a shows that the PSD values at $4.8 \le L^* < 4.9$ gradually decrease for the 4 hours prior to the dropout, which is also visible in the outermost portions of the PSD profiles in Figures 4a-c. This behaviour, along with the temporal evolution of the PSD profiles, is consistent with radial diffusion non-adiabatically transporting particles inward and therefore decreasing the population at higher L^* . The LCDS is located at $L^* \sim 7.5$ between 1:00–4:00, after which it begins to gradually move inward. The peak LCDS value before this compression was $L^* \sim 8.2$ and occurred at time 3:55. There are only two PSD data points at $4.8 \le L^* < 4.9$ after the LCDS compression begins, demonstrating that the population at most distant L^* are lost quickly after this point. The second and final PSD datapoint at $4.8 \le L^* < 4.9$ following the LCDS compression occurred at 4:25. Therefore, the entire electron population at $4.8 \le$ $L^* < 4.9$ was eliminated in 30 min, as determined from the time between the final PSD datapoint in this L^* range and the time of the peak LCDS value prior to the compression.

The PSD at $4.5 \le L^* < 4.6$, shown in Figure 5b, demonstrates a different temporal evolution. A similar gradual decrease in the PSD magnitude from midnight to approximately 4:00 can also be seen between $4.5 \le L^* < 4.6$, although with significantly more variation in the magnitude of the PSD than at $4.8 \le L^* < 4.9$. This population has PSD data points in the $4.5 \le L^* < 4.6$ range until $\sim 6:00$, until the LCDS has compressed to approximately $L^* \sim 5.5$. We note that the data density following the LCDS compression was significantly lower than beforehand, going from 18 data points between 2:00-4:00 to 6 data points between 4:00-6:00; this decrease in data density combined with the PSD profiles in 4days - g demonstrate that there was a depletion in the mid- L^* flux before 6:00 but not total elimination. The final PSD datapoint at $4.5 \le L^* < 4.6$ following the LCDS compression (but before the recovery that began after 8:00) occurred at 6:01. Based on the time offset between the initiation of the LCDS compression (3:55) and the final PSD datapoint in this L^* range (6:01), the electron population at $4.5 \le L^* < 4.6$ was eliminated in 126 min; slower than the loss at more distant L^* , which is consistent with magnetopause compression driving the dropout event.

By contrast, the PSD at the innermost L^* range (Figure 5c) does not show any depletion during the dropout event. In fact, the PSD between $4.2 \le L < 4.3$ has a gradual increase over the 12 h period shown in Figure 5, although we note that the PSD magnitude varies over this time period. This indicates that the innermost portion of the belt was relatively unaffected, which is again consistent with magnetopause compression driving the dropout as this loss mechanism would act faster and more effectively on particles that are nearest to the magnetopause.

These results show that the PSD loss heavily depended on both L^* and time. The most distant PSD was lost very quickly after the beginning of the inward compression of the LCDS, while the PSD in the mid- L^* range was not eliminated until the LCDS moved more significantly inward and the innermost PSD was unaffected by the compression of the LCDS. These results are again the most consistent with magnetopause shadowing as the dominant loss mechanism that acted to eliminate radiation belt particles at decreasing L^* as outer

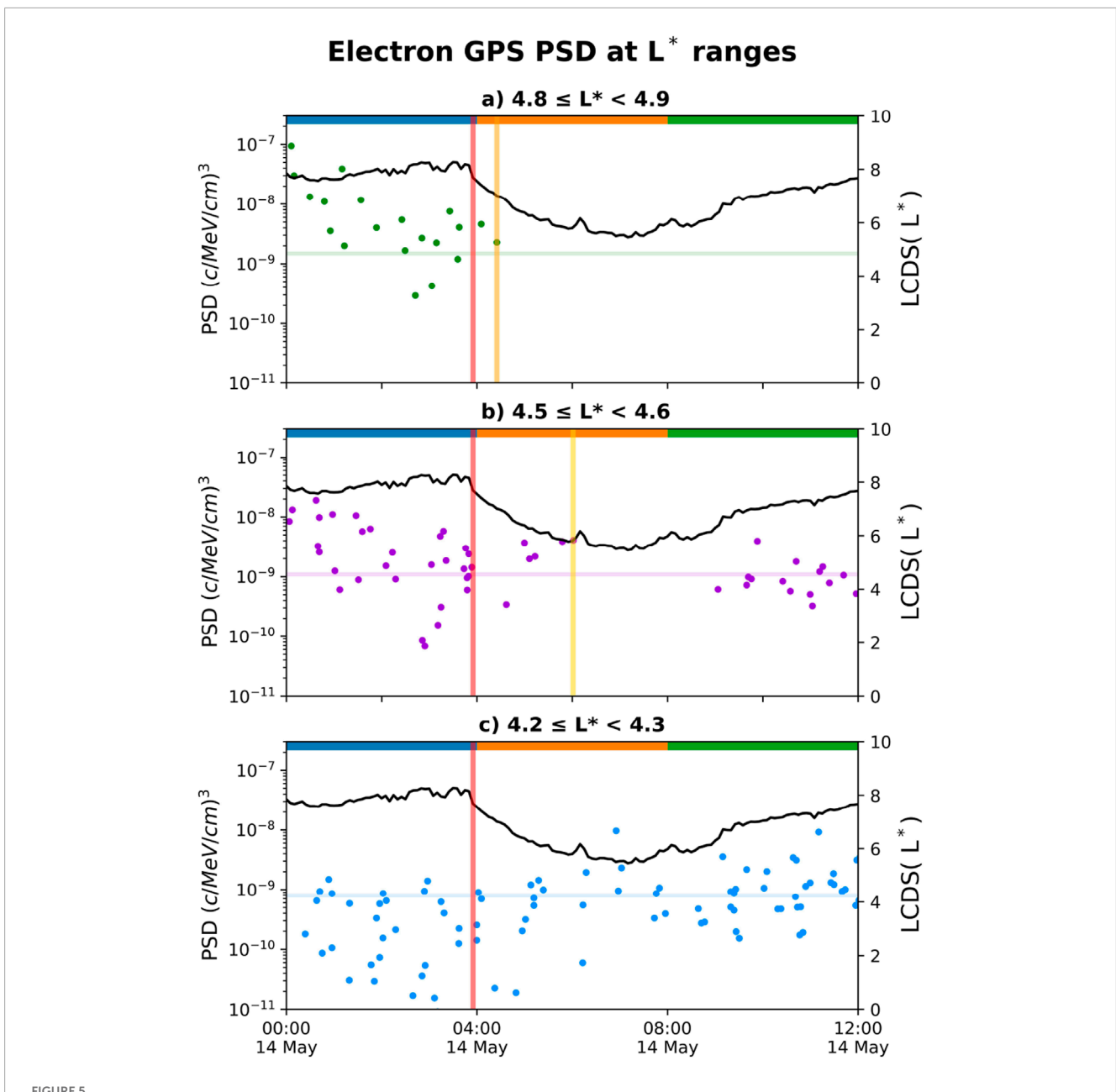


FIGURE 5
Temporal evolution of the electron PSD in different L^* ranges (left axis) in comparison to the LCDS calculated with $K = 0.14 R_E G^{1/2}$ (black, right axis), with shaded regions highlighting the L^* range that is shown in each subplot. Three vertical lines mark key points in the PSD evolution. The red line (located at 3:55) marks the beginning of the LCDS compression. The orange line in subplot a marks the last data point for the upper L* range (4:25), and the gold line in subplot b marks the last data point for the mid L* range (6:01). (a) $4.8 \le L * < 4.9$. (b) $4.5 \le L * < 4.6$. (c) $4.2 \le L * < 4.3$.

boundary of the radiation belt was compressed further inward. The most rapid loss occurred at the highest L^* , with the population at $4.8 \le L^* < 4.9$ being eliminated in only 30 min following the beginning of the LCDS compression.

5 Conclusion

A strong radiation belt dropout occurred on 14 May 2019, during a moderate geomagnetic storm. This affected all electron populations >0.8 MeV, although we focused on the 4 MeV

population for our analysis. The 4 MeV electron flux loss observed by the GPS constellation was rapid and closely corresponded to a strong magnetopause incursion, which occurred during a brief period of strongly southward IMF. The electron fluxes remained depleted for several hours and did not begin to recover until the IMF rotated northward and the magnetopause returned to its nominal location. The fluxes at L < 5 rapidly recovered to levels close to or greater than the pre-dropout fluxes when the magnetopause returned to its initial location, but the fluxes at more distant L-shell remained significantly depleted. Furthermore, the electron PSD profiles underwent a dramatic change in the shape of the profile

and the extent of the profile in L^* at the time of the magnetopause incursion. The PSD profiles were truncated in L^* and developed a steep gradient at the time of the magnetopause incursion, which is consistent with strong loss due to magnetopause shadowing. The timing of the dropout is L^* -dependent; the PSD at distant L^* were eliminated within half an hour while the population at mid- L^* took 2 hours to be entirely eliminated but experienced significant depletion soon after the LCDS compression began.

Sub-hour radiation belt dropouts are exceptionally rapid. Radiation belt dropouts are widely recognised as occurring on timescales of a few hours (Turner and Ukhorskiy, 2020, and references within), and dropouts on timescales of ≤ 2 hours are generally understood to be very fast, such as those discussed in Morley et al. (2010), Mourenas et al. (2016). The fastest dropout previously reported occurred on 21 March 2017, which may have occurred in as little as 10 min Kurita et al. (2018). We note however that Kurita et al. (2018) determined the 10-min loss timescale by inferring that the dropout began at the same time that EMIC waves were observed by ground based magnetometers; in-situ electron flux data from multi-constellation observations could only constrain this dropout to ≤ 1.5 hours. Loss timescales on the order of 0.5 - 2 hours were identified from in-situ data during dropouts that occurred during intense geomagnetic storms by Olifer et al. (2018), which also used the GPS constellation. The event reported in this study is one of only a small number of sub-hour dropout events that have been identified and is therefore among the fastest dropout events reported in the literature. This evaluation of exceptionally rapid, system-wide losses from the radiation belts was enabled through the GPS constellation, which provides observations of the radiation belts with extremely high data density, highlighting the value of constellations with many satellites to evaluate fast, system wide dynamics in the radiation belts.

Data availability statement

Publicly available datasets were analyzed in this study. This data can be found here: https://www.ngdc.noaa.gov/stp/space-weather/satellite-data/satellite-systems/lanl_gps/version_v1.10/.

Author contributions

AH: Formal Analysis, Visualization, Writing – original draft, Writing – review and editing, Investigation. HG: Formal Analysis, Visualization, Writing – original draft, Writing – review and editing, Conceptualization, Methodology, Supervision. MK: Data curation, Formal Analysis, Writing – review and editing. LO: Data curation, Formal Analysis, Writing – review and editing.

References

Albert, J. M., Selesnick, R. S., Morley, S. K., Henderson, M. G., and Kellerman, A. C. (2018). Calculation of last closed drift shells for the 2013 GEM radiation belt challenge events. *J. Geophys. Res. Space Phys.* 123, 9597–9611. doi:10.1029/2018JA025991

Funding

The author(s) declare that financial support was received for the research and/or publication of this article. This research was supported by the Boulder Solar Alliance Research Experience for Undergraduates Program, funded by the National Science Foundation, Award #1950911.

Acknowledgements

We thank Aaron Hendry and Sergio Vidal-Luengo for providing information on the relativistic electron precipitation signatures detected by their algorithms on the day of this dropout event.

Conflict of interest

The authors declare that the research was conducted in the absence of any commercial or financial relationships that could be construed as a potential conflict of interest.

Generative AI statement

The author(s) declare that no Generative AI was used in the creation of this manuscript.

Any alternative text (alt text) provided alongside figures in this article has been generated by Frontiers with the support of artificial intelligence and reasonable efforts have been made to ensure accuracy, including review by the authors wherever possible. If you identify any issues, please contact us.

Publisher's note

All claims expressed in this article are solely those of the authors and do not necessarily represent those of their affiliated organizations, or those of the publisher, the editors and the reviewers. Any product that may be evaluated in this article, or claim that may be made by its manufacturer, is not guaranteed or endorsed by the publisher.

Supplementary material

The Supplementary Material for this article can be found online at: https://www.frontiersin.org/articles/10.3389/fspas.2025.1694836/full#supplementary-material

Alken, P., Thébault, E., Beggan, C. D., Amit, H., Aubert, J., Baerenzung, J., et al. (2021). International geomagnetic reference field: the thirteenth generation. *Earth, Planets Space* 73, 49. doi:10.1186/s40623-020-01288-x

Baker, D. N., Erickson, P. J., Fennell, J. F., Foster, J. C., Jaynes, A. N., and Verronen, P. T. (2017). Space weather effects in the earth's radiation belts. *Space Sci. Rev.* 214, 17. doi:10.1007/s11214-017-0452-7

- Bentley, S. N., Stout, J. R., Thompson, R. L., Ratliff, D. J., and Watt, C. E. J. (2024). Two methods to analyze radial diffusion ensembles: the perils of space- and time-dependent diffusion. $Phys.\ Plasmas\ 31,\ 112901.\ doi:10.1063/5.0217268$
- Borovsky, J. E., and Denton, M. H. (2009). Relativistic-electron dropouts and recovery: a superposed epoch study of the magnetosphere and the solar wind. *J. Geophys. Res. Space Phys.* 114. doi:10.1029/2008JA013128
- Carson, B. R., Rodger, C. J., and Clilverd, M. A. (2013). POES satellite observations of EMIC-Wave driven relativistic electron precipitation during 1998–2010. *J. Geophys. Res. Space Phys.* 118, 232–243. doi:10.1029/2012JA017998
- Chen, Y., Friedel, R. H. W., Henderson, M. G., Claudepierre, S. G., Morley, S. K., and Spence, H. E. (2014). REPAD: an empirical model of pitch angle distributions for energetic electrons in the Earth's outer radiation belt. *J. Geophys. Res. Space Phys.* 119, 1693–1708. doi:10.1002/2013JA019431
- Cohen, I. J., Mauk, B. H., Anderson, B. J., Westlake, J. H., Sibeck, D. G., Turner, D. L., et al. (2017). Statistical analysis of mms observations of energetic electron escape observed At/beyond the dayside magnetopause. *J. Geophys. Res. Space Phys.* 122, 9440–9463. doi:10.1002/2017JA024401
- Cowley, S. W. H., and Lockwood, M. (1992). Excitation and decay of solar wind-driven flows in the magnetosphere-ionosphere system. *Ann. Geophys.* 10, 103–115. Available online at: https://ui.adsabs.harvard.edu/abs/1992AnGeo..10..103C/abstract.
- Dai, L., Wang, C., Duan, S., He, Z., Wygant, J. R., Cattell, C. A., et al. (2015). Near-earth injection of mev electrons associated with intense dipolarization electric fields: van allen probes observations. *Geophys. Res. Lett.* 42, 6170–6179. doi:10.1002/2015GL064955
- Dai, L., Han, Y., Wang, C., Yao, S., Gonzalez, W., Duan, S., et al. (2023). Geoeffectiveness of Interplanetary alfvén waves. I. Magnetopause magnetic reconnection and directly driven substorms. *Astrophysical J.* 945, 47. doi:10.3847/1538-4357/acb267
- Dai, L., Zhu, M., Ren, Y., Gonzalez, W., Wang, C., Sibeck, D., et al. (2024). Global-scale magnetosphere convection driven by dayside magnetic reconnection. *Nat. Commun.* 15, 639. doi:10.1038/s41467-024-44992-y
- Drozdov, A. Y., Allison, H. J., Shprits, Y. Y., Usanova, M., Saikin, A., and Wang, D. (2022). Depletions of multi-mev electrons and their association to minima in phase space density. *Geophys. Res. Lett.* 49, e2021GL097620. doi:10.1029/2021GL097620
- Fairfield, D. H. (1971). Average and unusual locations of the earth's magnetopause and bow shock. *J. Geophys. Res.* (1896-1977) 76, 6700–6716. doi:10.1029/JA076i028p06700
- Fu, W. D., Fu, H. S., Zhang, W. Z., Yu, Y., and Cao, J. B. (2025). Compression of earth's magnetopause Down to 5 re during the superstorm on 10 may 2024. $Geophys.\ Res.\ Lett.$ 52, e2024GL114040. doi:10.1029/2024GL114040
- George, H., Reeves, G., Cunningham, G., Kalliokoski, M. M. H., Kilpua, E., Osmane, A., et al. (2022). Contributions to loss across the magnetopause during an electron dropout event. *J. Geophys. Res. Space Phys.* 127, e2022JA030751. doi:10.1029/2022JA030751
- Grandin, M., Aikio, A. T., and Kozlovsky, A. (2019). Properties and geoeffectiveness of solar wind high-speed streams and stream interaction regions during solar cycles 23 and 24. *J. Geophys. Res. Space Phys.* 124, 3871–3892. doi:10.1029/2018JA026396
- Hartley, D. P., and Denton, M. H. (2014). Solving the radiation belt riddle. Astronomy & Geophys. 55, 6.17–6.20. doi:10.1093/astrogeo/atu247
- Hastings, D., and Garrett, H. (1996). *The space radiation environment*. Cambridge University Press: Cambridge Atmospheric and Space Science Series, 208–249.
- Henderson, M., Morley, S., Niehof, J., and Larsen, B. (2018). Drsteve/lanlgeomag: v1.5.16. doi:10.5281/zenodo.1195041
- Hendry, A. T., Rodger, C. J., Clilverd, M. A., Engebretson, M. J., Mann, I. R., Lessard, M. R., et al. (2016). Confirmation of EMIC wave-driven relativistic electron precipitation. *J. Geophys. Res. Space Phys.* 121, 5366–5383. doi:10.1002/2015JA022224
- Hendry, A. T., Rodger, C. J., and Clilverd, M. A. (2017). Evidence of submev emic-driven electron precipitation. *Geophys. Res. Lett.* 44, 1210–1218. doi:10.1002/2016GL071807
- Horne, R. B., Glauert, S. A., Kirsch, P., Heynderickx, D., Bingham, S., Thorn, P., et al. (2021). The satellite risk prediction and radiation forecast system (sarif). *Space weather.* 19, e2021SW002823. doi:10.1029/2021SW002823
- Kalliokoski, M. M. H., Henderson, M. G., Morley, S. K., Kilpua, E. K. J., Osmane, A., Olifer, L., et al. (2023). Outer radiation belt flux and phase space density response to sheath regions: Van Allen probes and GPS observations. *J. Geophys. Res. Space Phys.* 128, e2022JA030708. doi:10.1029/2022JA030708
- Kim, H.-J., and Chan, A. A. (1997). Fully adiabatic changes in storm time relativistic electron fluxes. *J. Geophys. Res. Space Phys.* 102, 22107–22116. doi:10.1029/97JA01814
- Koskinen, H. E. J., and Kilpua, E. K. J. (2022). *Physics of earth's radiation belts*. Springer International Publishing. doi:10.1007/978-3-030-82167-8

Kurita, S., Miyoshi, Y., Shiokawa, K., Higashio, N., Mitani, T., Takashima, T., et al. (2018). Rapid loss of relativistic electrons by EMIC waves in the outer radiation belt observed by arase, Van Allen probes, and the PWING ground stations. *Geophys. Res. Lett.* 45 (12), 720–12. doi:10.1029/2018GL080262

- $Lanzerotti,\ L.\ J.,\ and\ Baker,\ D.\ N.\ (2017).\ Space\ weather\ research:\ earth's\ radiation\ belts.\ \textit{Space weather.}\ 15,742-745.\ doi:10.1002/2017SW001654$
- Li, W., Shen, X.-C., Ma, Q., Capannolo, L., Shi, R., Redmon, R. J., et al. (2019). Quantification of energetic electron precipitation driven by plume whistler mode waves, plasmaspheric hiss, and exohiss. *Geophys. Res. Lett.* 46, 3615–3624. doi:10.1029/2019GL082095
- Loto'aniu, T. M., Singer, H. J., Waters, C. L., Angelopoulos, V., Mann, I. R., Elkington, S. R., et al. (2010). Relativistic electron loss due to ultralow frequency waves and enhanced outward radial diffusion. *J. Geophys. Res. Space Phys.* 115. doi:10.1029/2010JA015755
- Ma, Q., Li, W., Zhang, X. J., Bortnik, J., Shen, X. C., Connor, H. K., et al. (2021). Global survey of electron precipitation due to hiss waves in the earth's plasmasphere and plumes. *J. Geophys. Res. Space Phys.* 126, e2021JA029644. doi:10.1029/2021JA029644
- Madanian, H., Gingell, I., Chen, L.-J., and Monyek, E. (2024). Drivers of magnetic field amplification at oblique shocks: *in situ* observations. *Astrophysical J. Lett.* 965, L12. doi:10.3847/2041-8213/ad3073
- Milan, S., Wild, J., Grocott, A., and Draper, N. (2006). Space- and ground-based investigations of solar wind–magnetosphere–ionosphere coupling. *Adv. Space Res.* 38, 1671–1677. doi:10.1016/j.asr.2005.08.009
- Morley, S. K., Friedel, R. H. W., Cayton, T. E., and Noveroske, E. (2010). A rapid, global and prolonged electron radiation belt dropout observed with the global positioning system constellation. *Geophys. Res. Lett.* 37. doi:10.1029/2010GL042772
- Morley, S. K., Sullivan, J. P., Henderson, M. G., Blake, J. B., and Baker, D. N. (2016). The global positioning system constellation as a space weather monitor: comparison of electron measurements with Van allen probes data. *Space weather.* 14, 76–92. doi:10.1002/2015SW001339
- Morley, S. K., Sullivan, J. P., Carver, M. R., Kippen, R. M., Friedel, R. H. W., Reeves, G. D., et al. (2017). Energetic particle data from the global positioning system constellation. *Space weather.* 15, 283–289. doi:10.1002/2017SW001604
- Mourenas, D., Artemyev, A. V., Ma, Q., Agapitov, O. V., and Li, W. (2016). Fast dropouts of multi-MeV electrons due to combined effects of EMIC and whistler mode waves. *Geophys. Res. Lett.* 43, 4155–4163. doi:10.1002/2016GL068921
- Olifer, L., Mann, I. R., Morley, S. K., Ozeke, L. G., and Choi, D. (2018). On the role of last closed drift shell dynamics in driving fast losses and Van Allen radiation belt extinction. *J. Geophys. Res. Space Phys.* 123, 3692–3703. doi:10.1029/2018JA025190
- Olifer, L., Morley, S. K., Ozeke, L. G., Mann, I. R., Kalliokoski, M. M. H., Henderson, M. G., et al. (2024). Rapid acceleration bursts in the Van allen radiation belt. *J. Geophys. Res. Space Phys.* 129, e2024JA032544. doi:10.1029/2024JA032544
- Ozeke, L. G., Mann, I. R., Murphy, K. R., Sibeck, D. G., and Baker, D. N. (2017). Ultra-relativistic radiation belt extinction and ulf wave radial diffusion: modeling the September 2014 extended dropout event. *Geophys. Res. Lett.* 44, 2624–2633. doi:10.1002/2017GL072811
- Ozeke, L. G., Mann, I. R., Olifer, L., Dufresne, K. Y., Morley, S. K., Claudepierre, S. G., et al. (2020). Rapid outer radiation belt flux dropouts and fast acceleration during the March 2015 and 2013 storms: the role of ultra-low frequency wave transport from a dynamic outer boundary. *J. Geophys. Res. Space Phys.* 125, e2019JA027179. doi:10.1029/2019JA027179
- Papitashvili, N. E., and King, J. H. (2020). Omni 5-min data. doi:10.48322/gbpg-5r77
- Pham, K. H., Tu, W., and Xiang, Z. (2017). Quantifying the precipitation loss of radiation belt electrons during a rapid dropout event. *J. Geophys. Res. Space Phys.* 122 (10), 287–10. doi:10.1002/2017JA024519
- Reeves, G. D., Spence, H. E., Henderson, M. G., Morley, S. K., Friedel, R. H. W., Funsten, H. O., et al. (2013). Electron acceleration in the heart of the van allen radiation belts. *Science* 341, 991–994. doi:10.1126/science.1237743
- Shue, J.-H., Song, P., Russell, C. T., Steinberg, J. T., Chao, J. K., Zastenker, G., et al. (1998). Magnetopause location under extreme solar wind conditions. *J. Geophys. Res. Space Phys.* 103, 17691–17700. doi:10.1029/98JA01103
- Smirnov, A. G., Berrendorf, M., Shprits, Y. Y., Kronberg, E. A., Allison, H. J., Aseev, N. A., et al. (2020). Medium energy electron flux in earth's outer radiation belt (MERLIN): a machine learning model. *Space weather.* 18, e2020SW002532. doi:10.1029/2020SW002532
- Staples, F. A., Kellerman, A., Murphy, K. R., Rae, I. J., Sandhu, J. K., and Forsyth, C. (2022). Resolving magnetopause shadowing using multimission measurements of phase space density. *J. Geophys. Res. Space Phys.* 127, e2021JA029298. doi:10.1029/2021JA029298
- Su, Z., Gao, Z., Zheng, H., Wang, Y., Wang, S., Spence, H. E., et al. (2017). Rapid loss of radiation belt relativistic electrons by emic waves. *J. Geophys. Res. Space Phys.* 122, 9880–9897. doi:10.1002/2017JA024169
- Tsyganenko, N. A. (1989). A magnetospheric magnetic field model with a warped tail current sheet. *Planet. Space Sci.* 37, 5–20. doi:10.1016/0032-0633(89)90066-4

Tsyganenko, N. A., and Sitnov, M. I. (2005). Modeling the dynamics of the inner magnetosphere during strong geomagnetic storms. *J. Geophys. Res. Space Phys.* 110. doi:10.1029/2004JA010798

Turner, D. L., and Ukhorskiy, A. Y. (2020). "Chapter 1 - outer radiation belt losses by magnetopause incursions and outward radial transport: new insight and outstanding questions from the Van allen probes era," in *The dynamic loss of earth's radiation belts*. Editors A. N. Jaynes, and M. E. Usanova (Elsevier), 1–28.

Turner, D. L., Shprits, Y., and Angelopoulos, V. (2012). Explaining sudden losses of outer radiation belt electrons during geomagnetic storms. Nat. Phys. 8, 208-212. doi:10.1038/nphys2185

Turner, D. L., Angelopoulos, V., Morley, S. K., Henderson, M. G., Reeves, G. D., Li, W., et al. (2014). On the cause and extent of outer radiation belt losses during the 30 September 2012 dropout event. *J. Geophys. Res. Space Phys.* 119, 1530–1540. doi:10.1002/2013JA019446

Usanova, M. E., Drozdov, A., Orlova, K., Mann, I. R., Shprits, Y., Robertson, M. T., et al. (2014). Effect of emic waves on relativistic and ultrarelativistic electron populations: ground-based and van allen probes observations. *Geophys. Res. Lett.* 41, 1375–1381. doi:10.1002/2013GL059024

Vidal-Luengo, S. E., Blum, L. W., Bruno, A., Ficklin, A. W., de Nolfo, G., Guzik, T. G., et al. (2024). Characterization of relativistic electron precipitation events observed by the calet experiment using self-organizing-maps. *J. Geophys. Res. Space Phys.* 129, e2024JA032481. doi:10.1029/2024JA032481

Xiang, Z., Tu, W., Li, X., Ni, B., Morley, S. K., and Baker, D. N. (2017). Understanding the mechanisms of radiation belt dropouts observed by van allen probes. *J. Geophys. Res. Space Phys.* 122, 9858–9879. doi:10.1002/2017JA024487

Xiang, Z., Tu, W., Ni, B., Henderson, M. G., and Cao, X. (2018). A statistical survey of radiation belt dropouts observed by van allen probes. *Geophys. Res. Lett.* 45, 8035–8043. doi:10.1029/2018GL078907

Zhang, X.-J., Li, W., Thorne, R. M., Angelopoulos, V., Ma, Q., Li, J., et al. (2016). Physical mechanism causing rapid changes in ultrarelativistic electron pitch angle distributions right after a shock arrival: evaluation of an electron dropout event. *J. Geophys. Res. Space Phys.* 121, 8300–8316. doi:10.1002/2016JA022517

Zou, Z., Zuo, P., Ni, B., Gao, Z., Wang, G., Zhao, Z., et al. (2020). Two-step dropouts of radiation belt electron phase space density induced by a magnetic cloud event. Astrophysical J. Lett. 895, L24. doi:10.3847/2041-8213/ab9179